How to cite: *Angew. Chem. Int. Ed.* **2020**, *59*, 13004–13012
International Edition: doi.org/10.1002/anie.202004083
German Edition: doi.org/10.1002/ange.202004083

Ferroelasticity **Hot Paper**

Super- and Ferroelastic Organic Semiconductors for Ultraflexible Single-Crystal Electronics

Sang Kyu Park[+], Hong Sun[+], Hyunjoong Chung, Bijal B. Patel, Fengjiao Zhang, Daniel W. Davies, Toby J. Woods, Kejie Zhao, and Ying Diao**

Abstract: *Like silicon, single crystals of organic semiconductors are pursued to attain intrinsic charge transport properties. However, they are intolerant to mechanical deformation, impeding their application in flexible electronic devices. Such contradictory properties, namely exceptional molecular ordering and mechanical flexibility, are unified in this work. We found that bis(triisopropylsilylethynyl)pentacene (TIPS-P) crystals can undergo mechanically induced structural transitions to exhibit superelasticity and ferroelasticity. These properties arise from cooperative and correlated molecular displacements and rotations in response to mechanical stress. By utilizing a bending-induced ferroelastic transition of TIPS-P, flexible single-crystal electronic devices were obtained that can tolerate strains (ε) of more than 13 % while maintaining the charge carrier mobility of unstrained crystals ($\mu > 0.7\,\mu_0$). Our work will pave the way for high-performance ultraflexible single-crystal organic electronics for sensors, memories, and robotic applications.*

Introduction

Electronic materials require flexibility in order to accomplish conformal integration on nonplanar dynamic surfaces such as skins, internal organs, and textiles for wearable and implantable devices. Mechanical flexibility of electronic materials has been achieved by geometrical engineering of hard materials (e.g., wavy and serpentine patterns,[1] kirigami[2]) or by molecular design of intrinsically deformable π-conjugated polymers.[3,4] The latter approach is further amenable to large-scale, low-cost solution processing. However, the high intrinsic deformability of π-conjugated polymers is attained at the expense of reduced crystallinity and/or conjugation length, either through the synthetic approach to introduce dynamic bonds[5–7] or through nanoconfinement to enhance chain dynamics.[8–10] On the other hand, exceptional molecular ordering is the primary requirement for disorder-free charge transport. Towards this end, single crystals or long-range-ordered crystalline films of organic semiconductors have been pursued, achieving charge carrier mobilities above $10\,cm^2V^{-1}s^{-1}$ for both small molecules and polymers.[11–15] Despite their promising performances, single crystals or crystalline films are not tolerant to large mechanical deformation. It has been revealed that strain allows a shift towards non-equilibrium packing within the elastic deformation regime (the strain window limited up to about ±2 %); strain above this limit leads to brittle fractures.[16,17]

How can molecular crystals be rendered reversibly deformable beyond the elastic limit? An intriguing strategy offered by biological systems is the contractible tail of the bacteriophage T4 virus. Its tail sheath comprises a protein crystal capable of a cooperative structural transition to reach a staggering 60 % contraction; this transition is promoted by the concerted displacement and tilting of constituting proteins.[18,19] This fascinating deformation mechanism, known as a martensitic transformation, underlies (thermo)mechanically induced phase transitions and lattice reorientations of shape memory alloys.[20,21] This intriguing feature has also been discovered very recently in molecular crystals.[22–30] For instance, Takamizawa and co-workers demonstrated the superelasticity of terephthalamide based on a reversible transition between two mechanically interconvertible polymorphs.[22] In another example, it was demonstrated by the same group that mechanical shear induced twinning in 5-chloro-2-nitroaniline crystals, which reversed back upon shear loading in the opposite direction (i.e., ferroelasticity).[24] Aside from superelasticity and ferroelasticity, shape memory effects have also been observed. One example is the mechanical bending of terephthalic acid crystals, which resulted in metastable polymorphic structures whose shapes and structures were recovered through thermal treatment.[25] However, these remarkable superelastic and ferroelastic properties have not been discovered in electronic materials nor utilized as deformation mechanisms in flexible devices.

Herein, we present the first example of superelasticity and ferroelasticity in single crystals of a high-performance organic semiconductor, bis(triisopropylsilylethynyl)pentacene (TIPS-P). Comprehensive experimental studies and atomistic modeling were used to elucidate the key molecular basis for the emergence of these properties as highly concerted and

[*] S. K. Park,[+] H. Chung, B. B. Patel, F. Zhang, D. W. Davies, Y. Diao
Department of Chemical and Biomolecular Engineering
University of Illinois Urbana-Champaign
600 S. Mathews Avenue, Urbana, IL 61801 (USA)
E-mail: yingdiao@illinois.edu
H. Sun,[+] K. Zhao
School of Mechanical Engineering, Purdue University
West Lafayette, IN 47907 (USA)
E-mail: kjzhao@purdue.edu
T. J. Woods
School of Chemical Sciences
University of Illinois Urbana-Champaign
600 S. Mathews Avenue, Urbana, IL 61801 (USA)
[+] These authors contributed equally to this work.
Supporting information and the ORCID identification number(s) for the author(s) of this article can be found under: https://doi.org/10.1002/anie.202004083.

correlated rotations of the conjugated backbone. We further analyzed the formation of metastable polymorphs at the transition interface that mediates mechanically induced structural transitions—a mechanism not reported before. By harnessing a bending-induced ferroelastic transition in TIPS-P, we generated flexible single-crystal electronics that can withstand recoverable strains of over 13 %, well exceeding the state-of-the-art 2–3 % strain reported in the literature.[16,17,31–34] Indeed, this work represents the first demonstration of highly deformable single-crystal electronic devices enabled by stress-releasing cooperative structural transitions.

Results and Discussion

Mechanically Induced Cooperative Structure Transitions

As shown in Figure 1, we have discovered mechanically induced cooperative structural transitions in TIPS-P single crystals, which offer versatile pathways to accommodate large mechanical strain. Figure 1 a and b illustrate the superelastic transformations (red curve in Figure 1 d) of TIPS-P based on $[\bar{1}00]$-shear loading, either by Form II–I (b) or by Form III–II transitions. Upon mechanical loading (i–ii, Figure 1 a), a stable polymorph of TIPS-P crystal exhibits a strongly bent shape because of a shear-induced polymorphic transition to a metastable polymorph, which spontaneously straightens back by the reverse structural transition when the force is removed (iii–i′). As the process does not involve remnant strain, the stress–strain loop manifests in its closed form (Figure 1 d). We note that structural changes incurred during a superelastic transition are equivalent to a thermoelastic transition between a high-temperature and a low-temperature polymorph (Figure S1 a).

Moreover, two types of ferroelastic transformations are discovered in all polymorphs (Forms I, II, and III); the first type results from [100]-shear loading and the other types are a result of uniaxial tension along [010]. Micrographs in Figure 1 c describe a ferroelastic transformation based on [100]-shear loading (blue stress–strain curve in Figure 1 d). Mechanical shear induces the formation of twin domains that stay in place (i–ii) until reverse shear restores the original structure (iii–i′). As the deformed state is preserved after the shear stress has been removed (ii), the presence of remnant strain will be seen as an open stress–strain loop in this case (positive stress region of the blue stress–strain curve). However, the twinned domain can be restored back to the original structure by reverse loading, showing mechanical reversibility.

Molecular Mechanism of Superelasticity

We surmised that a prerequisite for superelasticity is the existence of thermally induced reversible martensitic transitions, that is, thermoelasticity.[35,36] Towards elucidating the structural origin of the observed superelasticity, we first mapped the temperature-dependent polymorphic phase space of TIPS-P single crystals by cross-polarized optical microscopy (CPOM), differential scanning calorimetry (DSC), and single-crystal X-ray diffraction (SC-XRD; Figures S1–S5). We observed three reversible polymorphic transitions involving four polymorphs, namely I—Ib, Ib–II, and II–III (Figure S1), consistent with our previous reports of polymorph transitions in thin films.[37] All transitions are single-crystal to single-crystal in nature showing a dramatic length change of the crystal (Figure S1 b, Movie S1). The Ib–II, II–III transitions are abrupt and exhibit transition temperature hystereses (Figure S1 c, d) suggesting first-order martensitic transitions. The I–Ib transition is gradual, and exhibits no hysteresis indicating that the transition is second-order. This inference was further validated by DSC (Figure S2). Due to the second-order nature of the I–Ib transition, we categorized Forms I and Ib as one family, and they exhibit

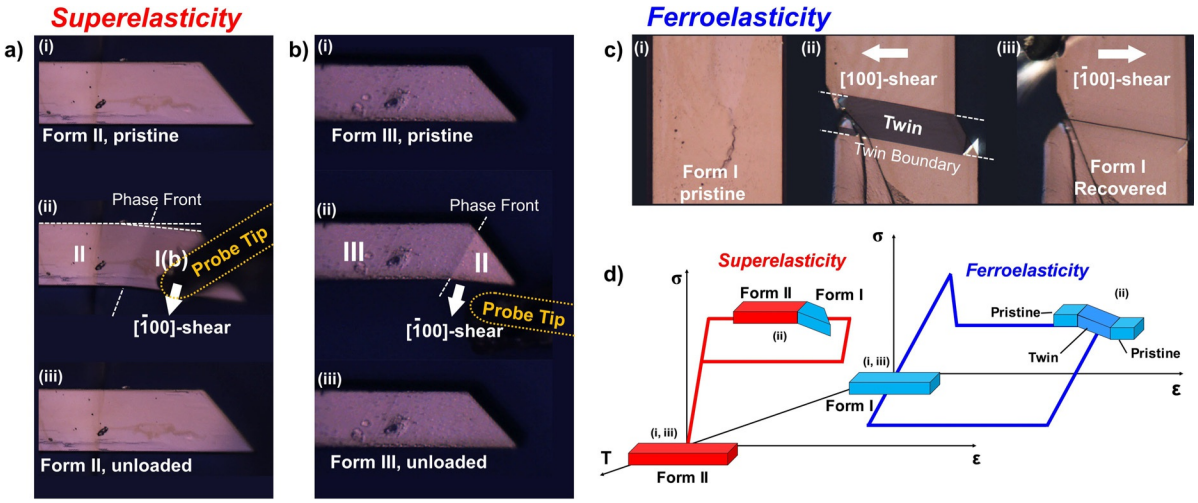

Figure 1. Mechanically induced structure transitions of TIPS-P single crystals. Micrographs that illustrate $[\bar{1}00]$-shear loading/unloading induced superelasticity: a) Form II–I(b) transition, SE1; b) Form III–II transition, SE2. c) [100]/$[\bar{1}00]$-shear loading induced ferroelasticity (deformation twinning/detwinning). We note that a phase front is observed in only some of the cases during the superelastic Form II–I(b) transition. d) Schematic temperature–stress–strain (T–σ–ε) curves to describe the states in the transition processes (i–iii) in (a) and (c).

only slight differences in their unit cell constants.[37] All of the polymorphs of TIPS-P show $P\bar{1}$ symmetry with a 2D-brickwork packing motif, but with a notable displacement of molecules along the π-plane (Figure S3). Moreover, from Form I to II and III, the side chain becomes increasingly more disordered (Figures S4, S5). Based on these structural characteristics, we inferred that the molecular origin of the thermoelastic transformations is the structural similarities between polymorphs[38–40] and order-to-disorder transitions of rotator side chains, consistent with our recent report.[41] The structural details of all polymorphs are presented in Figure S6.

Next, we show that thermoelastic transitions in TIPS-P crystals can also be triggered mechanically to give rise to a superelastic effect. Theoretically, superelasticity is a complete mechanical analogue to thermoelasticity. The interchangeability of temperature and stress effects is expressed by a Clausius–Clapeyron-type equation,[36]

$$\frac{d\sigma}{dT} = -\frac{\rho \Delta H}{T_0 \varepsilon} \quad (1)$$

where σ is the stress, T is the temperature, ρ is the density, ΔH is the enthalpic change, ε is the strain, and T_0 is the equilibrium transition temperature for the thermoelastic transition. To test if TIPS-P indeed exhibits superelasticity, we prepared free-standing crystals in a "jumping board" geometry (Scheme S1). The crystals were kept at 150 °C or 210 °C to examine stress-induced polymorph transitions of Forms II or III. Mechanical shear was applied using a micromanipulator tip. As the tip approaches the (100) facet, the crystals bend towards the probe tip as a result of electrostatic interactions, which corresponds to a shear deformation along the $[\bar{1}00]$ direction. Deformed crystals immediately regain their original shapes when the probe tip is removed (Movies S2, S3). The apparent shear deformation is accompanied by the appearance of a phase front separating the pristine and the deformed domains (Figure 1 a, b). This suggests that the large shear deformation is caused by a phase transition, rather than being due to the intrinsic elasticity of the crystal. We identified such phase transitions as superelastic transitions given the single-crystal to single-crystal nature and the reversibility of the transitions. This hypothesis was validated by CPOM (Figure 2 a) and Raman spectroscopy (Figure 2 c, d). These techniques collectively identified II–I(b) and III–II transitions when shearing Form II and III crystals, respectively, which we denote as SE1 and SE2. These results are discussed in detail below.

Figure 2 a shows micrographs upon SE1 and SE2 transformations, highlighting the characteristic crystallographic angle γ between the phase boundary (*a*-axis in Figure 2 b) and the long axis of the crystal (*b*-axis in Figure 2 b). In the case of SE1, the γ angles in the pristine and deformed regions are 72.2° and 80.3°, which correspond well to the angle between the (100) and (010) facets of Form II and I structures (γ in Figure 2 b), respectively. This result indicates that the deformed domain is Form I, which interfaces with the pristine Form II domain through the (010) plane as illustrated in Figure 2 b. As for SE1, the measured γ angles of SE2 (62.6° and 69.4° for pristine and deformed regions, respectively) correspond well to the angle between the (100) and (010) facets of Form III and II structures, indicating a III–II transformation. A (010) phase boundary is highly likely to occur, given that the area difference between the (010) planes of the pristine and the transformed polymorphs is negligibly small (0.6 % in SE1 and −0.4 % in SE2), thus leading to a small Bain distortion. The shear strains ($\gamma_{II}-\gamma_{I}$ and $\gamma_{III}-\gamma_{II}$ in radians) calculated for the SE1 and SE2 transformations are 17.3 % and 13.1 %, respectively.

The structural origins of the superelastic transitions were further evaluated by in situ Raman microscopy, which allowed us to identify local changes in structure upon polymorphic transition. As a phase descriptor, we focused on the characteristic frequency shift of the phonon vibration peak at approximately 86 cm^{-1} (*peak a* in Figure 2 c, d)—the frequencies in this region are sensitive to intermolecular interaction and packing changes.[42] The black spheres in Figure 2 c show the temperature-dependent frequency of this Raman mode (see the black spectra in Figure 2 d), exhibiting characteristic jumps from 85.7 to 83.7 cm^{-1} and from 83.7 to 81.4 cm^{-1} for II–I and III–II transitions, respectively. Interestingly, the position of *peak a* by $[\bar{1}00]$ shear shows approximately the same extent of shifts as in the thermoelastic transition (see the red and blue spheres for SE1 and SE2 in Figure 2 c, and the corresponding spectral changes in Figure 2 d). The result clearly points to Form II–I and III–II transitions by $[\bar{1}00]$-shear for SE1 and SE2, respectively.

The structural identification of SE1 (SE2), that is, a Form II–I(b) (III–II) transition bordering at the (010) plane, predicts a considerable rotation of the molecules by 12.0° (8.8°) and molecular displacement (Figure 2 b). Such a molecular mechanism in the superelastic transition was also captured by ab initio molecular dynamics (AIMD; see the Simulation Methods Section in the Supporting Information). We applied $[\bar{1}00]$-shear (un)loading onto the $2\times2\times1$ supercell of stable phases, Form II and III, which are stable at 127 °C and 227 °C (Figure 2 e). The molecules undergo a reversible concerted rotation by 11.9° (7.9°) upon SE1 (SE2) transition, in accordance with the shear (un)loading direction as depicted in Figures 2 e, S7, and S8. Cooperative displacive motions of the molecules along both the *y*- and *x*-axes are concurrent with the rotational motions, altering the solid-state molecular packing structure during the transformation (Figure S9, Table S1). In both the SE1 and SE2 transitions, length changes occur predominantly along the *b*-axis while the lengths of the *a*- and *c*-axes are well conserved, minimizing lattice distortion at the (010) interface and the energetic penalty of the transition. This superelastic nature is corroborated by the stress–strain hysteresis loop (Figure S10) with the stress plateau mediated by polymorphic transition. The small stress hysteresis suggests low energy dissipation, leading to excellent cyclic reversibility.

Molecular Mechanism of Ferroelasticity-1 (FE1)

In contrast to $[\bar{1}00]$-shear-induced superelasticity, applying the opposite [100]-shear onto Form I crystals led to

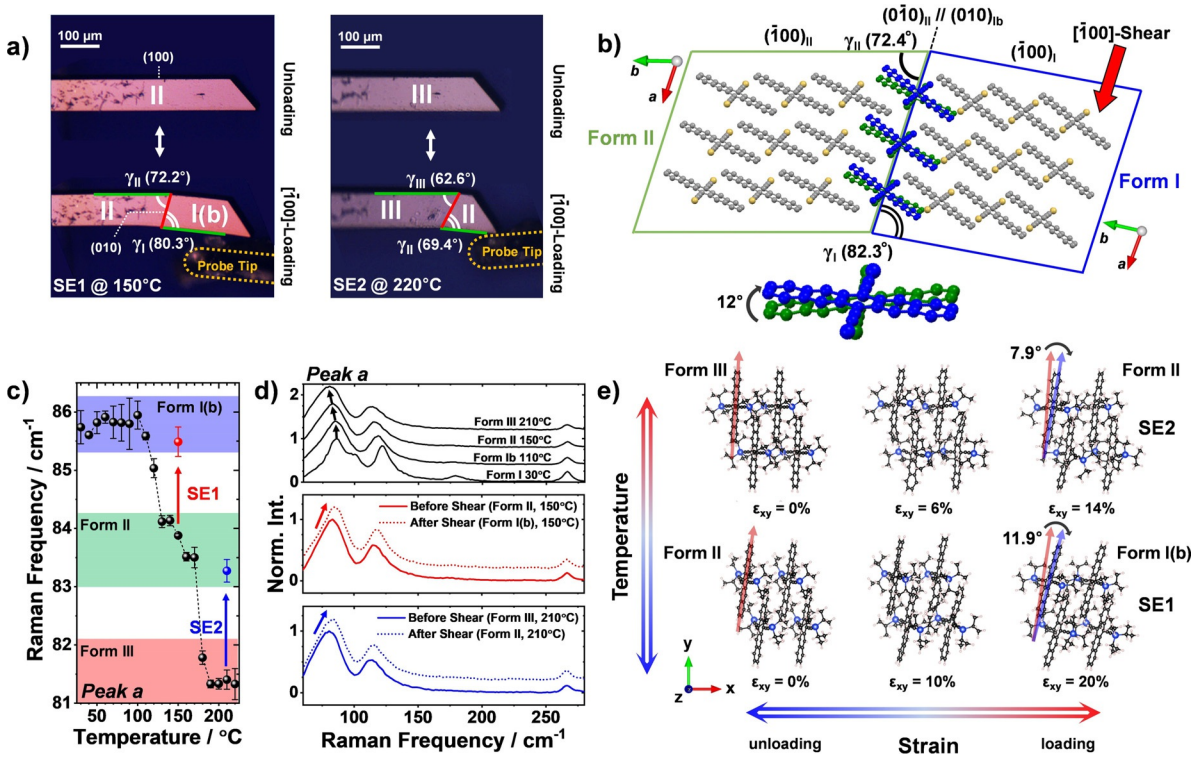

Figure 2. Superelasticity of TIPS-P single crystals. a) CPOM images taken before and after applying [1̄00]-shear onto single crystals of Form II at 150 °C (SE1, left) and Form III at 220 °C (SE2, right). Measured γ angles between the (100) and (010) planes are denoted for both pristine and deformed domains. b) The structural change upon SE1 transition (Form II–I), accomplished through loading and unloading [1̄00]-shear. The SE1 transition creates a (010) phase boundary between Form I and II domains resulting in a 12° molecular rotation. Coordinates in square brackets and parentheses denote directional vectors and planes, respectively. c) Temperature-dependent Raman frequency of *peak a* in (d) (black spheres), compared with frequency changes upon superelastic transformations at 150 °C (red sphere) and 210 °C (blue sphere). d) Representative Raman spectra recorded upon thermoelastic transition (black lines), SE1 (red solid line: before [1̄00]-shear, and red dotted line: after [1̄00]-shear), and SE2 (blue solid line: before [1̄00]-shear, and blue dotted line: after [1̄00]-shear). Arrows in the graphs indicate frequency changes of *peak a* upon application of shear. e) AIMD modeling of superelasticity induced by *x*-axis loading at 127 °C (SE1) and 227 °C (SE2). Simulated molecular orientation changes are indicated (SE1: 11.9° and SE2: 7.9°).

ferroelastic transitions and a large shape deformation (Figure 3a, b). We inferred the ferroelastic nature of the transition from the observation that the deformed crystals maintained their shape even after removing the shear stress; only upon reverse $[\bar{1}00]$-shear loading does the reverse transition occur to recover the original shape. Scanning electron microscopy (SEM) and atomic force microscopy (AFM) images of deformed crystals (Figure 3b, S11) show structural integrity despite the large deformation. We denote the [100]-shear-induced ferroelastic transition as FE1 hereafter. We note that FE1 occurs on all other polymorphs. Examples of FE1 for Forms Ib and II are shown in Movies S4, S5. Below we focus on FE1 of Form I for detailed structure characterizations.

We confirmed the structural basis of the ferroelasticity as a mechanically reversible twinning–detwinning process by SC-XRD (Figure S12). For FE1, the measured lattice constants of the pristine domain are consistent with the lattice constants of Form I (Figure S3). We attributed the slight deviation to plastic deformation upon shear.[25] Moreover, it was revealed that the deformed domain is a twin domain of the parent Form I polymorph. During shearing, the domain is reoriented by a 180° rotation about the (010) plane normal with $(010)_P//(0\bar{1}0)_T$ or $(0\bar{1}0)_P//(010)_T$ as the twin interface (Figure S12). We note that this orientation relationship is equivalent to a 42° rotation of the pentacene core (viewed along the *c*-axis) shown in Figure 3a. Such a molecular rotation was further confirmed by polarized Raman spectroscopy.[43] By measuring an angle-dependent intensity ratio of 1571 cm^{-1}/1369 cm^{-1}, we confirmed that the pentacene cores rotate by 40–50° (Figure 3c; see Supporting Text 1 for details).

Furthermore, SC-XRD revealed that the $(\bar{1}00)$ plane of the pristine crystal becomes a (110) plane in the twinned domain (Figure S12b, d). This observation led us to the important conclusion that a switching of the π-stacking axes occurred upon transformation, i.e., a switching between [010] and $[\bar{1}10]$ that results in an alteration of the side facets between $(\bar{1}00)$ and (110) planes (Figure 3a, b). Specifically, it is a reversible exchange of the main [010] and the secondary $[\bar{1}10]$ π-stacking axis in a 2D-brickwork structure. In other words, the molecular dimers in Figure S14 and S15 are converted from a [010]-pair into a $[\bar{1}10]$-pair and vice versa after the transition. The axis switching result from SC-XRD was affirmed by CPOM observations (see Supporting Text 2 for details). The alteration of the side facet between $(\bar{1}00)$ and

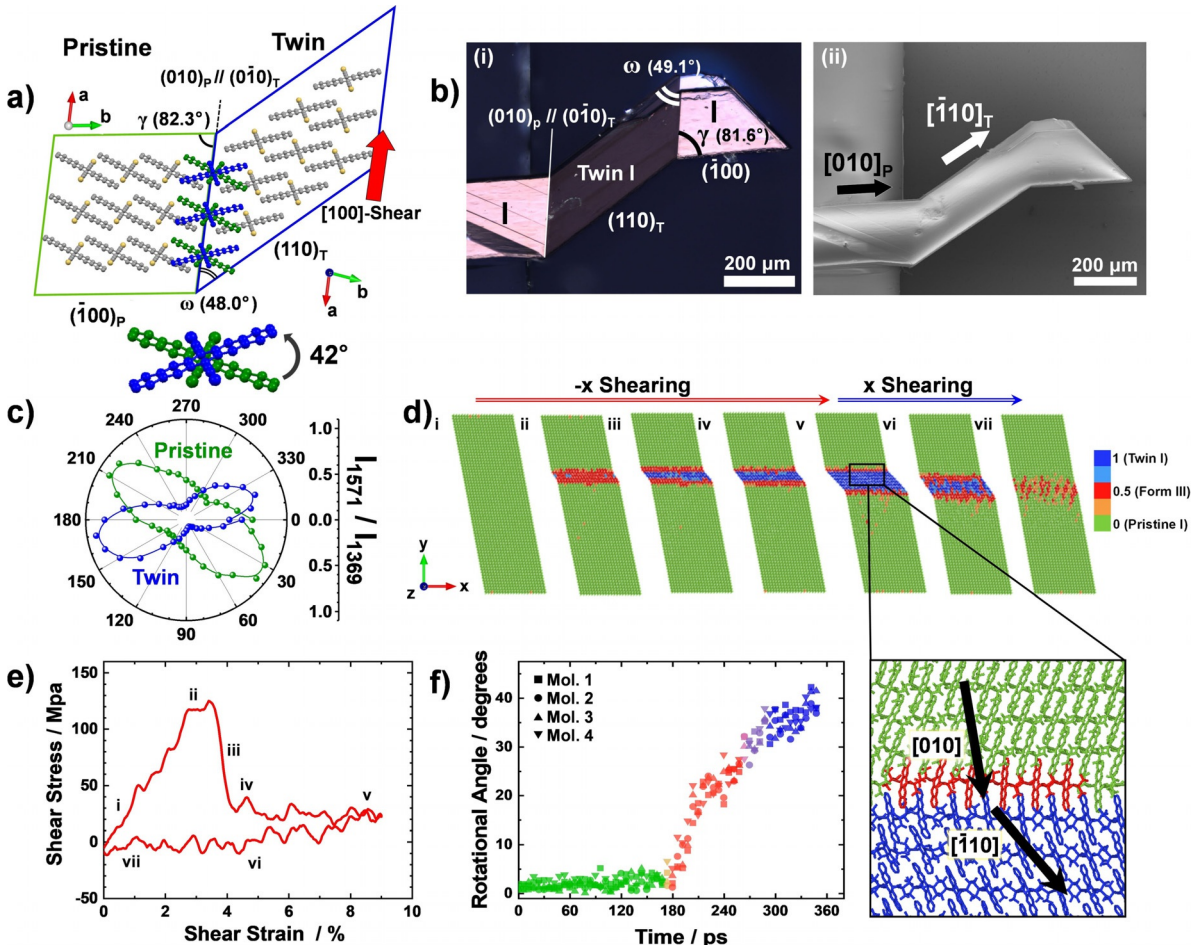

Figure 3. Ferroelasticity 1 (FE1) of TIPS-P crystals. a) Schematic illustration of the structural changes upon an FE1 transition (Form I) induced by [100]-shear loading. b) CPOM and SEM images of a TIPS-P crystal after [100]-shear-induced twin domain formation. Measured characteristic angles (γ and ω) are indicated in the CPOM image. The fracture-free nature of the FE1-induced deformation is revealed by SEM. c) Angle-dependent polarized Raman intensity ratio between the peaks at 1571 cm^{-1} and 1369 cm^{-1} (I_{1571}/I_{1369}) to confirm the molecular reorientation. d) Seven representative structural configurations generated during molecular dynamics simulations of the FE1 transition by [100]-shearing (*x*-axis) at 27 °C, and e) corresponding stress–strain loop. Original Form I (green) and twinned Form I (blue) states bridged by the intermediate Form III (red) at the interfacial (010) plane. Stacking axes switching is clearly shown in the magnified twinning interface in (d). f) Intralayer backbone rotation angle versus time plot of four different molecules in a molecular layer constituting the (010) plane, showcasing the cooperative nature of the transition by synchronized molecular rotation.

(110) predicts large theoretical recoverable strains up to 59.9 % and 25.5 % for Form I and II structures, respectively.

The molecular origin of twinning based on the FE1 mechanism was revealed by molecular dynamics (MD) simulations (see the Simulation Methods Section in the Supporting Information). The simulation not only predicts a switching of π-stacking axes upon transition (shown in the magnified view of Figure 3d), but also elucidates a layer-by-layer transition mechanism arising from intralayer molecular cooperativity. Figure 3d (Movie S6) shows representative structural configurations from the stress–strain loop in Figure 3e. The different phases in the simulation are color-coded in terms of the defined order parameter (Figure S16; see the Simulation Methods Section in the Supporting Information) ranging from 0 to 1 (green for Form I, red for intermediate Form III, and blue for twinned Form I). From configuration **i**–**ii**, the molecules glide along the shear direction with slight changes in the molecular orientation within the elastic deformation limit. Several molecular layers show counter-clockwise rotation by around 19°, promoting the alteration in the lattice symmetry and leading to a successive formation of intermediate Form III phases (red domains in configuration **ii**). This intermediate state shows structural neutrality between pristine and twinned structures in terms of their pentacene core orientations. This intermediate phase is conducive to nucleation of twinned domains by further shearing. Surpassing the transition onset (**ii**–**iv**), molecules in the intermediate regime continue to rotate up to 38° along with the translation of molecules along [100], resulting in the nucleation of twinned domains (blue zone) within the intermediate phase. The nucleated twinned structures rapidly spread through the entire intermediate phase and push Form III towards the interfaces between pristine and twinned domains (Figure S17). As a result, a dramatic stress relief is observed shown in Figure 3e. Further loading results in gradual layer-by-layer growth of twinned domains (**iv**–**v**). This

regime is represented by a plateau in Figure 3e, indicating that the transition becomes steady-state. By applying reverse shear along $[\bar{1}00]$ (**v**–**vii**), the twinned domain gradually recovers back to the intermediate phase (red) and then the original Form I (green), accompanied by clockwise molecular rotation by a total of 38°.

In addition to showing a layer-by-layer transition mechanism, the MD simulations also revealed molecular cooperativity during the FE1 transition. Figure 3 f shows a rotational angle versus time plot of four different molecules in a molecular layer, representing synchronized molecular rotation upon [100]-shear loading. Such concerted intralayer molecular rotation further promotes a correlated layer-by-layer transformation (Figure S18 and Movie S6). It is revealed in Figure S18 that the first layer starts the Form III–twinned I conversion as the second layer accomplishes the Form I–III transition; such synchronized rotation appears in all layers. The interlayer domino effect involving interfacial intermediate phase formation signifies the molecular origin for layer-by-layer processes of the FE1 transition as well as the molecular mechanism for alleviating stress at the twinning interface.

Molecular Mechanism of Ferroelasticity-2 (FE2)

Aside from the [100]-shear induced FE1 transition, a distinctive mechanically induced transition of Form I is observed upon applying uniaxial tension by bending (Figure 4a, b) or stretching along the [010] direction (Figure S19), which induces molecular displacements along the (210) plane. Such transformations occur in all polymorphs as they do in the FE1 case. As shown in Movie S7, we applied [010]-tension and compression by bending a Form I crystal attached to a deformable polyester terephthalate substrate (Scheme S1 c), which resulted in a reversible domain deformation. Performing SC-XRD on the deformed domain revealed an identical structure to the parent Form I polymorph (Figure S3) and confirmed the [010]-tension-induced deformation twinning (Figure S12) discussed in detail below. Therefore, we refer to this transition as FE2 hereafter. The SEM and AFM images in Figure 4b and S19 show the overall structural integrity during the FE2 transformation of a Form I crystal, but slight crack tip formation is observed at the crystal edges (Figure S21). This fracture would depreciate the charge transport characteristics in Form I crystals and cause device

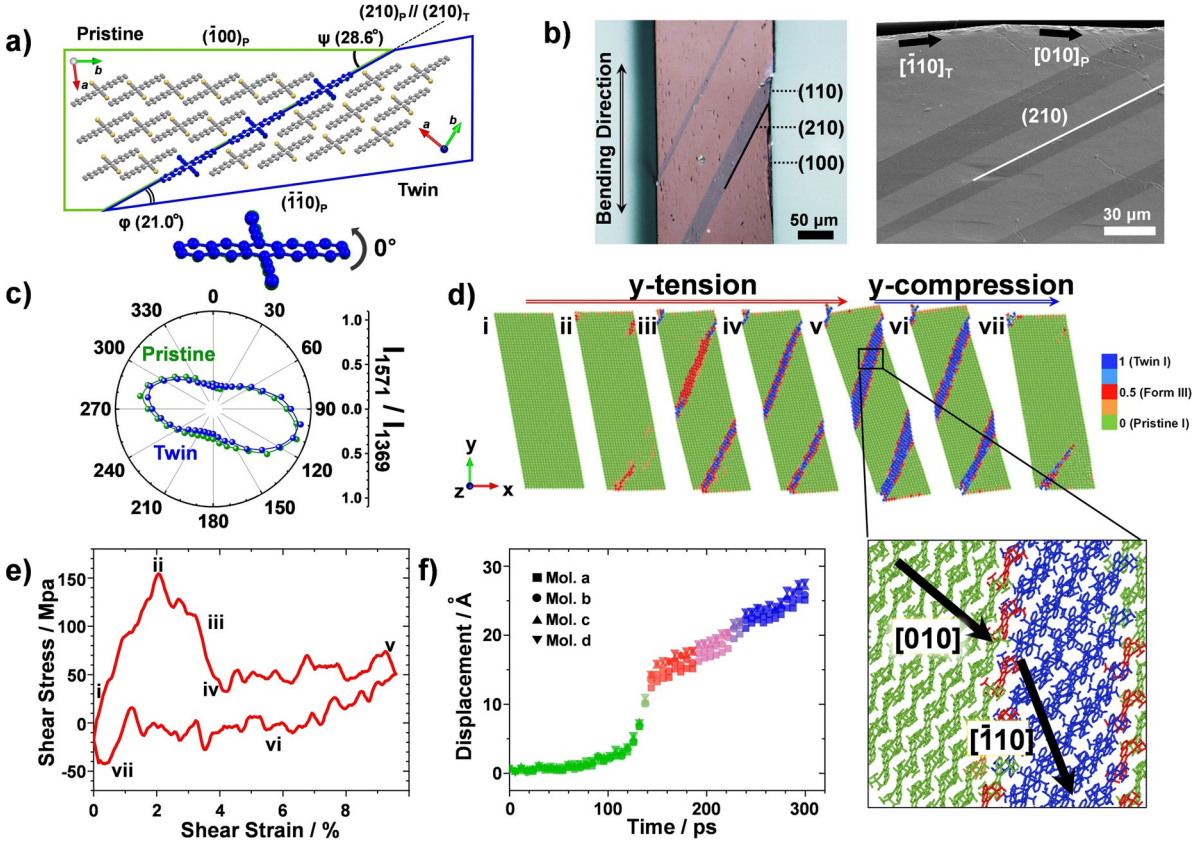

Figure 4. Ferroelasticity 2 (FE2) of TIPS-P crystals. a) Schematic illustration of the structural changes upon FE2 transition (Form I), induced by [010]-tension. The FE2 transition creates a twin boundary along the (210) plane and leads to an alteration of the habit plane from $(\bar{1}00)_P$ to $(110)_T$. b) CPOM and SEM images of TIPS-P crystals that have undergone an FE2 transition by [010]-tension. c) Angle-dependent polarized Raman intensity ratio between the peaks at 1571 cm^{-1} and 1369 cm^{-1} (I_{1571}/I_{1369}). d) Seven representative structural configurations generated during molecular dynamics simulations of the FE2 transition by [010]-tension (*y*-axis) at 27 °C, and e) the corresponding stress–strain loop. FE2 results in a transition from a pristine (green) to a twinned domain (blue) bridged by intermediate Form III (red) at the interfacial (210) plane. Magnified twinning interface of (d) shows axes switching through deformation twinning, i.e., [010] to $[\bar{1}10]$. f) Intralayer molecular displacement versus time plot of four different molecules in a molecular layer in the (210) plane, exhibiting cooperative nature.

failure at high strain. We show that such fractures can be prevented when inducing FE2 transitions from Form Ib crystals (see below).

Below, we present in detail the structural basis and molecular mechanism of the FE2 transition using Form I as an example; the transition was characterized by SC-XRD, CPOM, polarized Raman spectroscopy, and MD simulations. As in the case of FE1, performing SC-XRD allowed us to index the interfacial habit plane and to obtain the relative orientational relationship between pristine and deformed domains (Figure S12). Specifically, the interfacial habit plane of FE2 is indexed as (210), and the twinned lattice is reoriented by a 180° rotation about $[1\bar{2}0]$, which is parallel to the interfacial (210) plane. This lattice orientational relationship indicates only a very slight reorientation of the pentacene core by 2.2° with respect to the π-plane normal (Figure S22). Indeed, polarized Raman spectroscopy confirmed the preservation of the pentacene core orientation (Figure 4c). Lattice indexing results obtained by SC-XRD further revealed that the side $(\bar{1}00)$ facet of the pristine crystal changes into (110) for FE2, as in the FE1 case (Figure S12, Figure 4a). This suggests that axes switching between [010] and $[\bar{1}10]$ also occurs in FE2, which was validated by characteristic angle analysis through CPOM imaging (Supporting Text 2). Summarizing the above structural characterization results, we could envision molecular packing alterations at the interface as illustrated in Figure 4a, which shows that FE2 is accomplished by a significant molecular displacement along the (210) plane while preserving in-plane molecular orientations, contrary to the FE1 case. Based on this structure model, the theoretical recoverable strains of FE2 are 59.9% and 25.5% for Forms I and II, respectively (Figure S24).

We also carried out MD simulations by applying *y*-axis (i.e., approximately [010]) tension at 27°C on Form I, which exclusively resulted in FE2-based lattice reorientation (Figure 4d–f, Movie S8). As detailed in Supporting Text 3, tension along the *y*-axis engenders the FE2 transition by concerted molecular gliding parallel to the (210) interface. Like in the FE1 case, the simulated FE2 process also exhibits intermediate Form III layer formation and axis switching behavior.

Ultraflexible Single-Crystal Electronics

Mechanically induced cooperative structural transitions in the TIPS-P single crystals shown above can serve as a new mechanism for mitigating mechanical stress to realize ultraflexible single-crystal electronics. Especially related to the ferroelastic transformations, we have unveiled an exotic attribute of two-dimensional brickwork packing structures that can exchange π-stacking axes upon mechanical loading. In long-term studies of TIPS-P and its analogues, inherent two-dimensional electronic coupling and transport was revealed to contribute to high charge-carrier mobility owing to the two-dimensional brickwork packing.[37,44,45] This two-dimensional transport feature is based on the presence of two distinct charge-transport pathways, [010] as the primary transporting axis and $[\bar{1}10]$ as the secondary transporting axis in the TIPS-P case. We will show below that axes switching during ferroelastic transitions is capable of accommodating surprisingly large strains, while simultaneously mitigating the deterioration of the electronic performance by maintaining efficient transport pathways even after deformation.

For the first demonstration of molecular crystal electronics incorporating cooperative transitions, bendable TIPS-P single-crystal devices based on a two-channel configuration were fabricated. In the Type-1 test that measures the conductivity variation under stepwise enhancement of the tensile strain (Figures 5a, S25a, S26a, Table S2, and Scheme S3), we observed that a Form I crystal can maintain 70% of its initial conductivity ($\sigma/\sigma_0 \approx 0.7$) over the tensile strain range of 4.0–5.0%. Interestingly, even in a further extended state (around 5.8–9.3%), the σ/σ_0 values remained above 0.5 (Figure S26a). Furthermore, a slight increase in temperature to obtain a Form Ib structure (70–75°C) dramatically improved the crack-free transformation and conductivity, giving rise to σ/σ_0 values above 0.75 even at strains as high as 13.5% (Figure 5a, S26b, and Table S3). Moreover, we performed Type-2 tests on Form I crystal (Figure 5b, S25b and Table S4)—that is, conductivity characterization upon cyclic tensile loading, and observed that the conductivity values exhibit decent reversibility over five cycles over a strain range of $\varepsilon \approx 1.27$–2.52%. Our findings (black and red spheres in Figure 5a) show strikingly higher strain tolerance than for previously reported organic semiconductor single-crystal devices (Figure S27). Traditional molecular semiconductor crystals, which cannot extend beyond the elastic limit, exhibit steep reductions in charge carrier mobility even at very small tensile strains less than 2%, owing to prevalent brittle fracture. We attribute the high strain tolerance of our TIPS-P single crystals to the mechanically induced FE2 transitions.

A CPOM study performed in parallel confirmed the tension-induced FE2 transition and domain growth in both Form I and Ib single-crystal devices (Figure S28 and Figure 5c). Moreover, the crystals exhibit reversible thickening and thinning of twin domains upon strain cycling (Figure S29). However, in the highly strained states, a Form I crystal grows crack tips, which cause a significant drop in conductivity (Figure S28), while Form Ib crystals maintain both structural integrity and conductivity (Figure 5a,c; see Supporting Text 4 for details). We attribute the excellent strain tolerance of the conductivity to the preserved structural integrity as well as to the axes switching behavior, which provides an alternative transport pathway to the primary transport pathway upon the FE2 transition.

Conclusion

In conclusion, we have shown for the first time that single crystals of an organic semiconductor can be rendered ultraflexible by mechanically induced cooperative structural transitions, which act as a stress-release mechanism. We uncovered intralayer cooperativity and interlayer correlated molecular motions in TIPS-P crystals as the key molecular basis for attaining superelasticity and ferroelasticity. These mechanically induced transformations offer innate flexibility

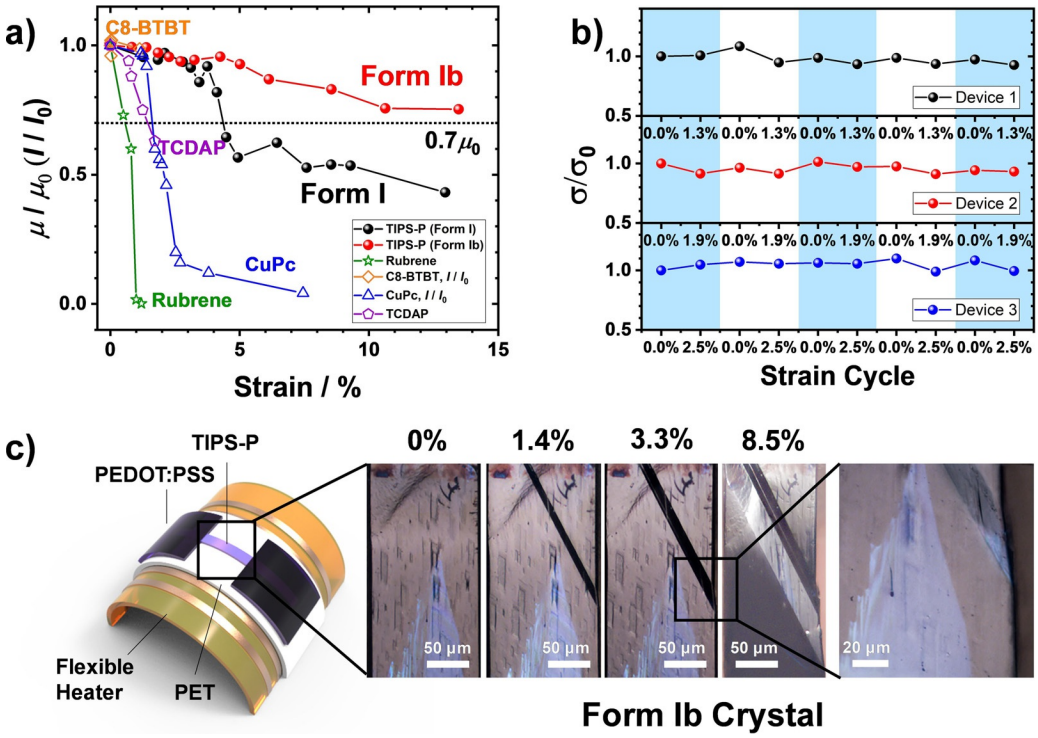

Figure 5. Flexible TIPS-P single-crystal device studies incorporating an FE2 transition. a) Tensile-strain-dependent mobility change (Type-1), measured on Form I (black) and Form Ib crystals (red). The results show significantly improved strain tolerance compared to those from reference molecular semiconductor crystals (green: rubrene, yellow: 2,7-dioctyl[1]benzothieno[3,2-*b*][1]benzothiophene (C8-BTBT), blue: copper(II) phthalocyanine (CuPc), purple: 5,7,12,14-tetrachloro-6,13-diazapentacene (TCDAP), Figure S26). b) Cycling tensile strain dependent mobility measurement (Type-2) using Form I single-crystal devices. c) Representative CPOM images of Form Ib crystals under Type-1 testing, showing that the FE2 transition occurs to mitigate bending stress and preserve the structural integrity during the transition.

and reversible deformability to semiconductor crystals. Our findings open a new avenue for developing single-crystal electronic devices that can significantly deform while maintaining structural integrity and carrier transport.

Acknowledgements

Y.D. acknowledges the Sloan Foundation for a Sloan Research Fellowship in Chemistry and a 3M Nontenured Faculty Award. S.K.P. acknowledges the Basic Science Research Program through the National Research Foundation of Korea (NRF) funded by the Ministry of Education (2017R1A6A3A03006242). H.S. and K.Z. acknowledge support from the National Science Foundation through grant CMMI-1941323. We thank Dr. SuYin Grass Wang, Dr. YuSheng Chen, and Tieyan Chang for help setting up the high-temperature single-crystal X-ray diffraction experiments, carried out at ChemMatCARS Sector, supported by the National Science Foundation under grant number NSF/CHE-1834750. This work was conducted in part in the Frederick Seitz Materials Research Laboratory Central Facilities, and at the Beckman Institute for Advanced Science and Technology at UIUC.

Conflict of interest

The authors declare no conflict of interest.

Keywords: ferroelasticity · Molecular electronics · phase transitions · polymorphism · superelasticity

[1] R. H. Kim, D. H. Kim, J. Xiao, B. H. Kim, S. I. Park, B. Panilaitis, R. Ghaffari, J. Yao, M. Li, Z. Liu, V. Malyarchuk, D. G. Kim, A. P. Le, R. G. Nuzzo, D. L. Kaplan, F. G. Omenetto, Y. Huang, Z. Kang, J. A. Rogers, *Nat. Mater.* **2010**, *9*, 929–937.
[2] M. K. Blees, A. W. Barnard, P. A. Rose, S. P. Roberts, K. L. McGill, P. Y. Huang, A. R. Ruyack, J. W. Kevek, B. Kobrin, D. A. Muller, P. L. McEuen, *Nature* **2015**, *524*, 204–207.
[3] S. E. Root, S. Savagatrup, A. D. Printz, D. Rodriquez, D. J. Lipomi, *Chem. Rev.* **2017**, *117*, 6467–6499.
[4] S. Wang, J. Y. Oh, J. Xu, H. Tran, Z. Bao, *Acc. Chem. Res.* **2018**, *51*, 1033–1045.
[5] C. Müller, S. Goffri, D. W. Breiby, J. W. Andreasen, H. D. Chanzy, R. A. J. Janssen, M. M. Nielsen, C. P. Radano, H. Sirringhaus, P. Smith, N. Stingelin-Stutzmann, *Adv. Funct. Mater.* **2007**, *17*, 2674–2679.
[6] J. Y. Oh, S. Rondeau-Gagne, Y. C. Chiu, A. Chortos, F. Lissel, G. N. Wang, B. C. Schroeder, T. Kurosawa, J. Lopez, T. Katsumata, J. Xu, C. Zhu, X. Gu, W. G. Bae, Y. Kim, L. Jin, J. W. Chung, J. B. Tok, Z. Bao, *Nature* **2016**, *539*, 411–415.
[7] G.-J. N. Wang, L. Shaw, J. Xu, T. Kurosawa, B. C. Schroeder, J. Y. Oh, S. J. Benight, Z. Bao, *Adv. Funct. Mater.* **2016**, *26*, 7254–7262.

[8] J. Xu, S. Wang, G.-J. N. Wang, C. Zhu, S. Luo, L. Jin, X. Gu, S. Chen, V. R. Feig, J. W. F. To, S. Rondeau-Gagné, J. Park, B. C. Schroeder, C. Lu, J. Y. Oh, Y. Wang, Y.-H. Kim, H. Yan, R. Sinclair, D. Zhou, G. Xue, B. Murmann, C. Linder, W. Cai, J. B.-H. Tok, J. W. Chung, Z. Bao, *Science* **2017**, *355*, 59 – 64.
[9] J. Xu, H. C. Wu, C. Zhu, A. Ehrlich, L. Shaw, M. Nikolka, S. Wang, F. Molina-Lopez, X. Gu, S. Luo, D. Zhou, Y. H. Kim, G. N. Wang, K. Gu, V. R. Feig, S. Chen, Y. Kim, T. Katsumata, Y. Q. Zheng, H. Yan, J. W. Chung, J. Lopez, B. Murmann, Z. Bao, *Nat. Mater.* **2019**, *18*, 594.
[10] G. Zhang, M. McBride, N. Persson, S. Lee, T. J. Dunn, M. F. Toney, Z. Yuan, Y.-H. Kwon, P.-H. Chu, B. Risteen, E. Reichmanis, *Chem. Mater.* **2017**, *29*, 7645 – 7652.
[11] V. C. Sundar, J. Zaumseil, V. Podzorov, E. Menard, R. L. Willett, T. Someya, M. E. Gershenson, J. A. Rogers, *Science* **2004**, *303*, 1644 – 1646.
[12] J. Takeya, M. Yamagishi, Y. Tominari, R. Hirahara, Y. Nakazawa, T. Nishikawa, T. Kawase, T. Shimoda, S. Ogawa, *Appl. Phys. Lett.* **2007**, *90*, 102120.
[13] Y. Yuan, G. Giri, A. L. Ayzner, A. P. Zoombelt, S. C. Mannsfeld, J. Chen, D. Nordlund, M. F. Toney, J. Huang, Z. Bao, *Nat. Commun.* **2014**, *5*, 3005.
[14] C. Luo, A. K. Kyaw, L. A. Perez, S. Patel, M. Wang, B. Grimm, G. C. Bazan, E. J. Kramer, A. J. Heeger, *Nano Lett.* **2014**, *14*, 2764 – 2771.
[15] E. Mohammadi, C. Zhao, F. Zhang, G. Qu, S. H. Jung, Q. Zhao, C. M. Evans, J. K. Lee, D. Shukla, Y. Diao, *ACS Appl. Mater. Interfaces* **2019**, *11*, 22561 – 22574.
[16] M. A. Reyes-Martinez, A. J. Crosby, A. L. Briseno, *Nat. Commun.* **2015**, *6*, 6948.
[17] T. Kubo, R. Hausermann, J. Tsurumi, J. Soeda, Y. Okada, Y. Yamashita, N. Akamatsu, A. Shishido, C. Mitsui, T. Okamoto, S. Yanagisawa, H. Matsui, J. Takeya, *Nat. Commun.* **2016**, *7*, 11156.
[18] G. B. Olson, H. Hartman, *J. Phys. (Paris)* **1982**, *43*, C4-855 – C4-865.
[19] A. A. Aksyuk, P. G. Leiman, L. P. Kurochkina, M. M. Shneider, V. A. Kostyuchenko, V. V. Mesyanzhinov, M. G. Rossmann, *EMBO J.* **2009**, *28*, 821 – 829.
[20] K. Otsuka, X. Ren, *Prog. Mater Sci.* **2005**, *50*, 511 – 678.
[21] J. F. Gómez-Cortés, M. L. Nó, I. López-Ferreño, J. Hernández-Saz, S. I. Molina, A. Chuvilin, J. M. San Juan, *Nat. Nanotechnol.* **2017**, *12*, 790 – 796.
[22] S. Takamizawa, Y. Miyamoto, *Angew. Chem. Int. Ed.* **2014**, *53*, 6970 – 6973; *Angew. Chem.* **2014**, *126*, 7090 – 7093.
[23] S. Takamizawa, Y. Takasaki, *Angew. Chem. Int. Ed.* **2015**, *54*, 4815 – 4817; *Angew. Chem.* **2015**, *127*, 4897 – 4899.
[24] S. H. Mir, Y. Takasaki, E. R. Engel, S. Takamizawa, *Angew. Chem. Int. Ed.* **2017**, *56*, 15882 – 15885; *Angew. Chem.* **2017**, *129*, 16098 – 16101.
[25] E. Ahmed, D. P. Karothu, M. Warren, P. Naumov, *Nat. Commun.* **2019**, *10*, 3723.
[26] D. P. Karothu, J. Weston, I. T. Desta, P. Naumov, *J. Am. Chem. Soc.* **2016**, *138*, 13298 – 13306.
[27] Z. S. Yao, M. Mito, T. Kamachi, Y. Shiota, K. Yoshizawa, N. Azuma, Y. Miyazaki, K. Takahashi, K. Zhang, T. Nakanishi, S. Kang, S. Kanegawa, O. Sato, *Nat. Chem.* **2014**, *6*, 1079 – 1083.
[28] S. Takamizawa, Y. Takasaki, *Chem. Sci.* **2016**, *7*, 1527 – 1534.
[29] S. Takamizawa, Y. Takasaki, T. Sasaki, N. Ozaki, *Nat. Commun.* **2018**, *9*, 3984.
[30] S. Sakamoto, T. Sasaki, A. Sato-Tomita, S. Takamizawa, *Angew. Chem. Int. Ed.* **2019**, *58*, 13722 – 13726; *Angew. Chem.* **2019**, *131*, 13860 – 13864.
[31] A. L. Briseno, R. J. Tseng, M.-M. Ling, E. H. L. Falcao, Y. Yang, F. Wudl, Z. Bao, *Adv. Mater.* **2006**, *18*, 2320 – 2324.
[32] J. Kang, J. Kim, J. W. Jo, J. S. Heo, M. G. Kim, Y. H. Kim, J. Kim, S. K. Park, *Small* **2017**, *13*, 1602467.
[33] W. Deng, X. Zhang, C. Gong, Q. Zhang, Y. Xing, Y. Wu, X. Zhang, J. Jie, *J. Mater. Chem. C* **2014**, *2*, 1314 – 1320.
[34] M. T. Ho, Y. T. Tao, *J. Vis. Exp.* **2016**, *117*, e54651.
[35] L. Delaey, R. V. Krishnan, H. Tas, H. Warlimont, *J. Mater. Sci.* **1974**, *9*, 1521 – 1535.
[36] P. Wollants, J. R. Roos, L. Delaey, *Prog. Mater. Sci.* **1993**, *37*, 227 – 288.
[37] Y. Diao, K. M. Lenn, W. Y. Lee, M. A. Blood-Forsythe, J. Xu, Y. Mao, Y. Kim, J. A. Reinspach, S. Park, A. Aspuru-Guzik, G. Xue, P. Clancy, Z. Bao, S. C. Mannsfeld, *J. Am. Chem. Soc.* **2014**, *136*, 17046 – 17057.
[38] M. K. Panda, T. Runčevski, A. Husain, R. E. Dinnebier, P. Naumov, *J. Am. Chem. Soc.* **2015**, *137*, 1895 – 1902.
[39] S. C. Sahoo, S. B. Sinha, M. S. R. N. Kiran, U. Ramamurty, A. F. Dericioglu, C. M. Reddy, P. Naumov, *J. Am. Chem. Soc.* **2013**, *135*, 13843 – 13850.
[40] M. K. Panda, T. Runčevski, S. C. Sahoo, A. A. Belik, N. K. Nath, R. E. Dinnebier, P. Naumov, *Nat. Commun.* **2014**, *5*, 4811.
[41] H. Chung, D. Dudenko, F. Zhang, G. D'Avino, C. Ruzie, A. Richard, G. Schweicher, J. Cornil, D. Beljonne, Y. Geerts, Y. Diao, *Nat. Commun.* **2018**, *9*, 278.
[42] A. J. Zaczek, L. Catalano, P. Naumov, T. M. Korter, *Chem. Sci.* **2019**, *10*, 1332 – 1341.
[43] D. T. James, B. C. Kjellander, W. T. Smaal, G. H. Gelinck, C. Combe, I. McCulloch, R. Wilson, J. H. Burroughes, D. D. Bradley, J.-S. Kim, *ACS Nano* **2011**, *5*, 9824 – 9835.
[44] A. Troisi, G. Orlandi, J. E. Anthony, *Chem. Mater.* **2005**, *17*, 5024 – 5031.
[45] K. J. Thorley, T. W. Finn, K. Jarolimek, J. E. Anthony, C. Risko, *Chem. Mater.* **2017**, *29*, 2502 – 2512.

Manuscript received: March 19, 2020
Accepted manuscript online: April 27, 2020
Version of record online: May 20, 2020

